Stability and accuracy analysis of wire-antenna modelling

van Schijndel, A.

Award date:
2004

TU/e technische universiteit eindhoven

Faculty of Electrical Engineering
Division Telecommunication Technology and Electromagnetics
Chair of Electromagnetics

Stability and accuracy analysis of wire-antenna modelling

by A. van Schijndel

EM-10-04

October, 2004

Report of Master's project performed at
TU/e, Electromagnetics Section and
TNO –FEL, The Hague

Supervisors:
Dr.ir. S.H.J.A. Vossen (TNO-FEL)
Prof.dr.ir. A.P.M. Zwamborn

Stability and accuracy analysis of wire-antenna modelling

A. van Schijndel

24th November 2004

Contents

Summary **5**

1 Introduction **7**
1.1 Determining input impedances of wire antennas 7
1.2 The scope of this thesis 8
1.3 Outline of this thesis 8

2 Model description **9**
2.1 Helmholtz equations 10
2.2 EM-interaction on a perfectly conducting object 10
2.3 Thin-wire equation 11
2.3.1 Reduced thin-wire kernel 12
2.3.2 Exact thin-wire kernel 13

3 Numerical implementation **15**
3.1 Method of Moments solution 15
3.2 Calculation of the system matrix 16
3.3 Basis and testing functions 18
3.4 Tackling the Green's function singularity 19
3.5 Source implementation 19

4 Validation of the developed code **21**
4.1 Squared cosine basis and testing functions 21
4.2 Triangle basis and testing functions 24
4.3 Thick wire, $L = 1.5$ m and $a = 5$ cm 26
4.4 Conclusions 27

5 Stability research **29**
5.1 Wire, $L = 0.5$ m and $a = 5$ mm 32
5.2 Thin wire, $L = 50$ m and $a = 1$ mm 32
5.3 Thick wire, $L = 0.5$ m and $a = 1.5$ cm 35
5.4 Conclusions 35

6 Conclusions and recommendations **37**
6.1 Conclusions 37
6.2 Recommendations 38

A Variables transformation **39**

B Matrix operations **41**
B.1 Picard criterion 41
B.2 Minimum Description Length (MDL) 41

Bibliography **42**

Summary

For special antenna geometries, it is known that numerical modelling techniques can produce inaccurate results. Although the numerical calculations were performed within a given numerical accuracy, it turned out that despite an increment in numerical accuracy, the results may still be wrong and therefore it is concluded that the modelling approach is not robust. The object of this master of science graduation project was to investigate accuracy and reliability aspects of the numerical analysis of wire antenna structures.

This research report begins with a theoretical description of the wire model in Chapter 2. In this chapter, the derivation of Pocklington's thin-wire equation is briefly demonstrated. Subsequently, in Chapter 3, the numerical implementation of the equation with the Moment Method is described.

The computer implementation of the theory is validated, in Chapter 4, against three available codes, namely NEC2, a Pocklington based code and a Hallén based code. The validation results gives us insight that the triangle basis and testing function produces the correct results. The squared cosine function does not produce the right answer because it did not match the current well at the end faces of the wire. The results from this chapter acknowledge that the reference codes are based on the "reduced kernel".

In order to gain insight in the reliability of the numerical implementation, research was performed into the stability and accuracy of the numerical implementation. This is presented in Chapter 5. The following checks didn't contribute to earlier findings or weren't providing information without comparing the results of the two kernels (EK and RK):

- The sorted singular values,
- The derivative of the singular values, non-sorted and sorted,
- The second derivate of the singular values,
- The FFT of the singular values,
- The FFT of the derivative of the singular values,
- The FFT of the current,
- The so-called Picard criterium,
- The so-called Minimum Description Length.

The finally implemented and used stability test determines the percentage of the number of singular values above a certain threshold. This threshold is chosen as the mean value of the singular values. If the percentage is more than 50 %, numerical test show that the solution is found to be stable. This last stability test gave a good indication of whether the approach is robust or not.

Chapter 1

Introduction

1.1 Determining input impedances of wire antennas

Designing antennas, one of the important characteristics that should be determined, is the input impedance. In the past, antenna modelling was based on experience and trial and error. In 1897 Pocklington present in his article [18], a differential equation from which the current along a thin wire antenna can be obtained. Solving Pocklington's equation wasn't numerically implemented, until appropriate computer resources became available. After this first article by Pocklington, several other methods were developed, e.g. Halléns equation [2, 15, 5] as result.

In the 1970's a discussion started about how to solve Pocklington's equation efficiently [4, 16, 17, 32]. Butler and Wilton came to the conclusion that the so-called collocation scheme converges badly and therefore they advised to use Garlerkin's method.

Jones started a more fundamental discussion [11] about which kernel in the integral equation should be used. The kernel represents the system description in the differential equation. Tijhuis *et al.* described in [23], that the reduced kernel can be derived exactly. Rynne explained in [19, 20], why the so called "exact kernel" is well-posed. Davies proposes in her article [8] how to calculate the "exact kernel" efficiently together with an appropriate solution method. Van Beurden explains in his thesis [25], the reason of the ill-posedness of the "reduced kernel". His conclusion is that near-field quantities should be determined with the "exact kernel" to obtain accurate results. Furthermore his derivation of the "exact kernel" is exact.

At the same time that the issues above were given attention, another discussion was going on, namely what is the best source model to be used. Tsai [24] gives an alternative for the widely used delta-gap excitation, namely the frill-source. This is also explained in Balanis [1, Section 8.3.3, p. 392-395]. In 1995 and 1996, Junker *et al.* gave an alternative for the two previous source models, the delta-gap and frill-source [12, 13, 14]. In 2000, Cui presented, in my opinion, a promising source model in [7].

1.2 The scope of this thesis

The input impedance is one of the important parameters while designing antennas. These antennas are placed on complex objects like planes, ships or vehicles. The analysis of appropriate design parameters is performed by using several numerical techniques implemented on computers. A number of them suffer from reliability problems, despite of what the commercial people or the programmers want you to believe. Therefore, the antenna designers are assisted by EM-specialists to be able to adequately interpret the results.

During one of the research projects at TNO-FEL, several EM-solvers have been compared to each other. From this study, it has been concluded that the computer programs don't suffice in all situations, because of several errors in the numerical implementation [26].

For special antenna geometries, it is known that numerical modelling produces inaccurate results. Although the numerical calculations are performed within a given numerical accuracy. It turned out that despite an increment in numerical accuracy, the results may still be wrong and therefore it is concluded that the modelling approach is not robust. The object of this master of science graduation project was to investigate accuracy and reliability aspects of the numerical analysis of wire antenna structures.

1.3 Outline of this thesis

This report starts with a theoretical description of the wire model in Chapter 2. In this chapter, the derivation of Pocklington's thin-wire equation is briefly demonstrated. In Chapter 3 the numerical implementation of the equation with the Method of Moment follows. The obtained numerical code is verified and validated in Chapter 4 for three interesting examples. In Chapter 5 the reliability of the answers produced by different wire kernels is investigated by addressing certain parameters. The last chapter, Chapter 6, provides the conclusions and recommendations.

Chapter 2

Model description

The electromagnetic problem that is solved is located in a homogeneous space and is a time invariant isotropic medium, in our case free space. In this medium there is a polarised quantity, defined as a vector, a quantity with a length and direction. The description is given for now in Cartesian coordinates. A location in the Cartesian reference frame is given by $\mathbf{x} = (x, y, z)$. The unit of time is denoted by t . For the frequency, f, the following interrelation is used $\omega = 2\pi f$.

The electric and magnetic field vectors, $\boldsymbol{\mathcal{E}}$ and $\boldsymbol{\mathcal{H}}$, respectively, are governed by Maxwell's equations in time domain,

$$\nabla \times \boldsymbol{\mathcal{E}} + \partial_t \boldsymbol{\mathcal{B}} = \mathbf{0}, \tag{2.1}$$
$$\nabla \times \boldsymbol{\mathcal{H}} - \partial_t \boldsymbol{\mathcal{D}} = \boldsymbol{\mathcal{J}}, \tag{2.2}$$

accompanied by the constitutive relations,

$$\nabla \cdot \boldsymbol{\mathcal{D}} = \rho, \tag{2.3}$$
$$\nabla \cdot \boldsymbol{\mathcal{B}} = 0. \tag{2.4}$$

The flux densities are defined as $\boldsymbol{\mathcal{D}} = \varepsilon_0 \boldsymbol{\mathcal{E}}$ and $\boldsymbol{\mathcal{B}} = \mu_0 \boldsymbol{\mathcal{H}}$.

To be able to perform our analysis in both time and frequency domain, we define the Fourier transformation as follows

$$F(\omega) = \int_{-\infty}^{\infty} \mathcal{F}(t) \exp(-\imath\omega t) dt, \tag{2.5}$$

$$\mathcal{F}(t) = \frac{1}{2\pi} \int_{-\infty}^{\infty} F(\omega) \exp(\imath\omega t) d\omega. \tag{2.6}$$

By applying Fourier transform on Equation (2.1) and (2.2), Maxwell's equations in frequency domain are written as:

$$\nabla \times \mathbf{E} + \imath\omega\mu_0 \mathbf{H} = \mathbf{0}, \tag{2.7}$$
$$\nabla \times \mathbf{H} - \imath\omega\varepsilon_0 \mathbf{E} = \mathbf{J}. \tag{2.8}$$

2.1 Helmholtz equations

From Maxwell's equations in frequency domain we take the divergence of Equation (2.7) and obtain

$$\nabla \cdot \mathbf{H} = 0. \tag{2.9}$$

With the aid of Equation (2.9) it is then easily verified that

$$\mathbf{H} = \nabla \times \mathbf{A}. \tag{2.10}$$

This combined with Equation (2.7) gives

$$\nabla \times \mathbf{E} + \imath\omega\mu_0 \nabla \times \mathbf{A} = \mathbf{0}. \tag{2.11}$$

From the latter equation the curl operator is removed and a gradient of a scalar function is added, because the curl of a gradient results in zero. Then we obtain

$$\mathbf{E} = -\imath\omega\mu_0 \mathbf{A} - \frac{\nabla\Phi}{\imath\omega\varepsilon_0}. \tag{2.12}$$

As a next step we substitute Equation (2.10) and (2.12) into Equation (2.8). This yields

$$\nabla \times \nabla \times \mathbf{A} - k_0^2 \mathbf{A} + \nabla\Phi = \mathbf{J}. \tag{2.13}$$

The latter equation combined with the Lorenz gauge:

$$\nabla \cdot \mathbf{A} = -\Phi, \tag{2.14}$$

provides us with the Helmholtz equations,

$$\nabla^2 \mathbf{A} + k_0^2 \mathbf{A} = -\mathbf{J}, \tag{2.15}$$

$$\nabla^2 \Phi + k_0^2 \Phi = \nabla \cdot \mathbf{J}, \tag{2.16}$$

$$\mathbf{E} = \frac{1}{\imath\omega\varepsilon_0} \left(\nabla\nabla \cdot \mathbf{A} + k_0^2 \mathbf{A}\right). \tag{2.17}$$

2.2 EM-interaction on a perfectly conducting object

To evaluate the EM-interaction of an arbitrary perfectly conducting object, as defined in Figure 2.1, the first step is to determine the surface current density $\mathbf{J}_S$. To this end, we first introduce the incident and scattered electric field $\mathbf{E}^i$ and $\mathbf{E}^s$, the interior of the object $\mathcal{D}$, the exterior of the object $\overline{\mathcal{D}}$ and the boundary between them $\partial\mathcal{D}$.

From Helmholtz equations, the total electric field and the incident field on a perfectly electrically conducting (PEC) object are interrelated as follows

$$\mathcal{S}_{\overline{\mathcal{D}}}(\mathbf{r})\, \mathbf{E}(\mathbf{r},\omega) - \mathbf{E}^i(\mathbf{r},\omega) = -\frac{1}{\imath\omega\varepsilon_0} \left[\nabla\Phi(\mathbf{r},\omega) - k_0^2 \mathbf{A}(\mathbf{r},\omega)\right] \tag{2.18}$$

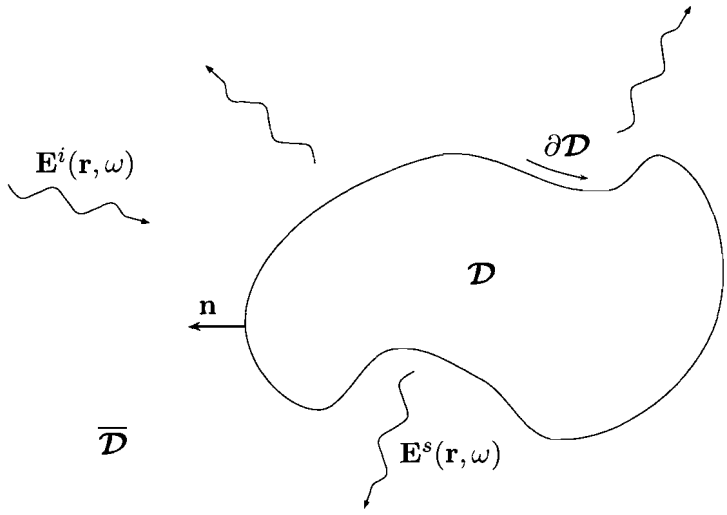

Figure 2.1: Domain definitions for the derivation of the integral equations.

where,

$$\Phi(\mathbf{r},\omega) = -\oint_{\mathbf{r}'\in\partial\mathcal{D}} G(R,\omega)\,\nabla'_S\cdot\mathbf{J}_S(\mathbf{r}',\omega)\,d\mathbf{r}', \tag{2.19}$$

$$\mathbf{A}(\mathbf{r},\omega) = \oint_{\mathbf{r}'\in\partial\mathcal{D}} G(R,\omega)\,\mathbf{J}_S(\mathbf{r}',\omega)\,d\mathbf{r}'. \tag{2.20}$$

Both the potential and the vector potential in Equation (2.19) and (2.20) are calculated by integrals with a convolutional structure over surface current density $\mathbf{J}_S$ and the Green's function

$$G(R,\omega) = \frac{\exp(-\imath k_0 R)}{4\pi R}, \tag{2.21}$$

where $R = |\mathbf{r}-\mathbf{r}'|$, $k_0 = \omega\sqrt{\varepsilon_0\mu_0}$ is the wave number and ∇_S is the surface divergence. The prime in the surface divergence indicates that the operator pertains to $\mathbf{r}'$. The shape function [22] is defined as

$$\mathcal{S}_{\overline{\mathcal{D}}} = \begin{cases} 0 & \mathbf{r}\in\mathcal{D} \\ \frac{1}{2} & \mathbf{r}\in\partial\mathcal{D} \\ 1 & \mathbf{r}\in\overline{\mathcal{D}} \end{cases}. \tag{2.22}$$

2.3 Thin-wire equation

Now we define our PEC object as a thin wire, see Figure 2.2, with L the length and a the radius of the wire. For using the thin-wire equation two constrains should be fullfilled: $a \ll L$ and $a \ll \lambda$. The thin-wire equation can easily be derived after defining the current in cylindrical coordinates,

$$I(z) = \int_0^{2\pi} \mathbf{J}_S(\phi,z)\cdot\mathbf{u}_z a\,d\phi, \tag{2.23}$$

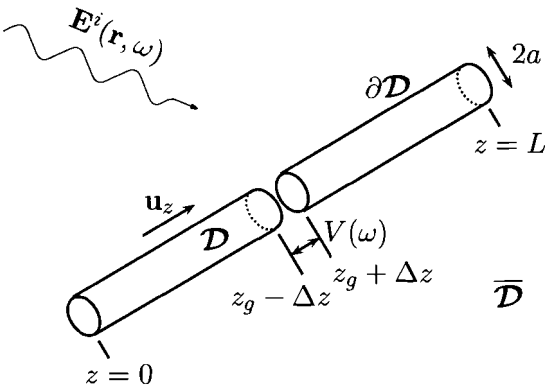

Figure 2.2: Wire geometry with incident field.

herein it is observed that the current only exist on the mantle of the wire, without a current on the end faces. This implies that the term $R = |\mathbf{r} - \mathbf{r}'|$ for $\mathbf{r}$ on $\partial\mathcal{D}$ can be written as

$$\begin{aligned} \left|\mathbf{r}-\mathbf{r}'\right|^2 &= \left|(r\cos\phi, r\sin\phi, z) - \left(r'\cos\phi', r'\sin\phi', z'\right)\right|^2 \\ &= 2a^2\left[1-\cos\left(\phi-\phi'\right)\right] + \left|z-z'\right|^2 \\ &= 4a^2\sin^2\tfrac{1}{2}\left(\phi-\phi'\right) + \left|z-z'\right|^2. \end{aligned} \tag{2.24}$$

The next step is to rewrite Equation (2.18) for the thin wire in cylindrical coordinates. This provides us with,

$$\begin{aligned} &\mathcal{S}_{\overline{\mathcal{D}}}(\mathbf{r})\, E_z(\mathbf{r},\omega) - E_z^i(\mathbf{r},\omega) = \\ &\qquad \frac{1}{\imath\omega\varepsilon_0}\left[\partial_z \int_0^L\int_0^{2\pi} G(R,\omega)\,\nabla'_S\cdot\mathbf{J}_S\left(\phi',z'\right) a d\phi' dz' \right. \\ &\qquad \left. +k_0^2\int_0^L\int_0^{2\pi} G(R,\omega)\,\mathbf{J}_S\left(\phi',z'\right)\cdot\mathbf{u}_z a d\phi' dz'\right], \end{aligned} \tag{2.25}$$

and

$$\nabla_S\cdot\mathbf{J}_S(\phi,z) = \frac{1}{a}\partial_\phi J_{S,\phi}(\phi,z) + \partial_z J_{S,z}(\phi,z). \tag{2.26}$$

From Equation (2.23), (2.25) and (2.26) can be extracted two possible solution approaches. These two will be discussed in the next subsections.

2.3.1 Reduced thin-wire kernel

The exact derivation, as proposed by Tijhuis [23], is to choose the observation point on the axis and the source point on the mantle of the wire. This yields

$$\begin{aligned} &\imath\omega\varepsilon_0\left[\mathcal{S}_{\overline{\mathcal{D}}}(\mathbf{r})\, E_z(z\mathbf{u}_z,\omega) - E_z^i(z\mathbf{u}_z,\omega)\right] = \\ &\partial_z\int_0^L K_R\left(z-z'\right)\partial_{z'} I\left(z'\right) dz' + k_0^2\int_0^L K_R\left(z-z'\right) I\left(z'\right) dz', \end{aligned} \tag{2.27}$$

which is referred to as Pocklington's equation with the "reduced kernel" defined as

$$K_R(z) = \frac{\exp\left(-\imath k_0 \sqrt{a^2+z^2}\right)}{2\sqrt{a^2+z^2}}. \tag{2.28}$$

2.3.2 Exact thin-wire kernel

The starting point is still Equation (2.23), (2.25) and (2.26). This is amended with the arguments from van Beurden [25]. ϕ'-Dependence of the integrated Green's function can be removed by integrating over a full period of ϕ because the Green's function G is a periodic function of $\phi - \phi'$. To ensure consistence between the left and right hand side of the equality sign in Equation (2.25), the E-fields will also be integrated over ϕ. The ϕ'-integration is now only for the current density and produces the the current, according to Equation (2.23). Hence, this gives us Pocklington's equation:

$$\begin{aligned} &\imath\omega\varepsilon_0 \left[\mathcal{S}_{\overline{\mathcal{D}}}(\mathbf{r}) \int_0^{2\pi} E_z(\mathbf{r},\omega)\, d\phi - \int_0^{2\pi} E_z^i(\mathbf{r},\omega)\, d\phi\right] = \\ &\partial_z \int_0^L K_E(z-z')\, \partial_{z'} I(z')\, dz' + k_0^2 \int_0^L K_E(z-z')\, I(z')\, dz', \end{aligned} \tag{2.29}$$

with

$$K_E(z) = \int_0^{2\pi} \frac{\exp\left(-\imath k_0 \sqrt{4a^2 \sin^2 \frac{1}{2}(\phi-\phi') + z^2}\right)}{4\pi\sqrt{4a^2 \sin^2 \frac{1}{2}(\phi-\phi') + z^2}} d(\phi-\phi') \tag{2.30}$$

$$= 4\int_0^{\frac{\pi}{2}} \frac{\exp\left(-\imath k_0 \sqrt{4a^2 \sin^2\phi + z^2}\right)}{4\pi\sqrt{4a^2 \sin^2\phi + z^2}} d\phi, \tag{2.31}$$

known as the "exact kernel". The $\mathbf{r}$ mentioned in the left hand side of Equation (2.29) is given by $\mathbf{r} = a\mathbf{u}_r(\phi) + z\mathbf{u}_z = a\cos(\phi)\mathbf{u}_x + a\sin(\phi)\mathbf{u}_y + z\mathbf{u}_z$, which denotes a point on the mantle of the wire.

Chapter 3

Numerical implementation

In this chapter the derivation is focussed to the "exact kernel". Hence, the equation to solve is (2.29), which can be written in operator notation as follows

$$L\,I = E^c, \tag{3.1}$$

in which the linear operator L works on $I(z)$ as

$$L\,I = \partial_z \int_0^L K_E\left(z - z'\right) \partial_{z'} I\left(z'\right) dz' + k_0^2 \int_0^L K_E\left(z - z'\right) I\left(z'\right) dz' \tag{3.2}$$

and the known quantity is given by

$$E^c = u\omega\varepsilon_0 \left[\mathcal{S}_{\overline{\mathcal{D}}}\left(\mathbf{r}\right) \int_0^{2\pi} E_z\left(\mathbf{r}, \omega\right) d\phi - \int_0^{2\pi} E_z^i\left(\mathbf{r}, \omega\right) d\phi \right]. \tag{3.3}$$

3.1 Method of Moments solution

The Method of Moments (MoM) [6, Chapter 4] starts by using a finite set of functions ψ_i with $i = 1, \ldots, N-1$, called the expansion or basis functions, which are used to construct an approximation of the current I in N equally approximated currents as:

$$I \approx I_N\left(z\right) = \sum_{i=1}^{N-1} \alpha_i \psi_i\left(z\right), \tag{3.4}$$

where the coefficients $\{\alpha_i\}$ are the unknowns to be determined. Substituting Equation (3.4) into Equation (3.1), and taking in account the linearity of the operator L, we obtain the following equation:

$$L\,I \approx L\,I_N\left(z\right) = \sum_{i=1}^{N-1} \alpha_i L\psi_i\left(z\right) \approx E^c\left(z\right),\ z \in \partial\mathcal{D} \tag{3.5}$$

The above equation is an approximation of Equation (3.1). It must be discretised so that it can be solved by a computer. To do this, a new set of functions W_j

with $j = 1, \ldots, N-1$, called the testing or weighting functions, is chosen. Then, taking the inner product of each weighting function with Equation (3.5) results in a system of linear algebraic equations:

$$\sum_{i=1}^{N-1} \alpha_i \langle L\psi_i, W_j \rangle = \langle E^c, W_j \rangle , \; j = 1, \ldots, N-1. \tag{3.6}$$

This equation can be written in matrix equation form as

$$[Z]\,[I] = [V] \tag{3.7}$$

with

$$Z_{ij} = \langle L\psi_i, W_j \rangle , \tag{3.8}$$

denotes the system matrix,

$$I_i = \alpha_i, \tag{3.9}$$

denotes the unknown current vector and

$$V_j = \langle E^c, W_j \rangle , \tag{3.10}$$

denotes the known Voltage quantities. The subscripts i and j are given by,

$$i = 1, \ldots, N-1 \wedge j = 1, \ldots, N-1.$$

Finally the inner product is defined as

$$\langle f, g \rangle = \int_{\partial \mathcal{D}} f(z) g^*(z) dz, \tag{3.11}$$

where the asterisk denotes the complex conjugate of $g(z)$.

3.2 Calculation of the system matrix

The expansion and weighting functions are chosen to be the same, $W_j = \psi_j$. This is referred to as Galerkin's method, which gives better results according to [4, 17, 32]. Then the vector $[V]$ becomes

$$V_j = \langle E^c, \psi_j \rangle = u\omega\varepsilon_0 \int_{z_{j-1}}^{z_{j+1}} \left[\mathcal{S}_{\overline{\mathcal{D}}} (\mathbf{r}) \int_0^{2\pi} E_z (\mathbf{r}, \omega)\, d\phi \right] \psi_j(z) dz, \tag{3.12}$$

when the incident field is absent. The weighting functions are defined on the domain $[z_{j-1}, z_{j+1}]$. The elements of the system matrix are given by

$$\begin{aligned} Z_{ij} = \langle L\psi_i, \psi_j \rangle = \int_{z_{j-1}}^{z_{j+1}} \Bigg[& \partial_z \int_{z_{i-1}}^{z_{i+1}} K_E (z - z')\, \partial_{z'} \psi_i (z')\, dz' + \\ & k_0^2 \int_{z_{i-1}}^{z_{i+1}} K_E (z - z')\, \psi_i (z')\, dz' \Bigg] \psi_j (z)\, dz. \end{aligned} \tag{3.13}$$

The wire is divided into smaller segments, where our testing points are chosen on the end of the segments. The wire is divided in N equally sized segments, therefore the segment length is $\Delta z = \frac{L}{N}$. The integration boundaries are given by

$$z_j = j\Delta z = \frac{jL}{N}, \tag{3.14}$$

$$z_i = i\Delta z = \frac{iL}{N}. \tag{3.15}$$

Equation (3.13) can be split up into two parts, one with the differentials the other without, then we get

$$Z_{ij} = Z_{ij}^d + Z_{ij}^r \tag{3.16}$$

where

$$Z_{ij}^d = \int_{z_{j-1}}^{z_{j+1}} \left[\partial_z \int_{z_{i-1}}^{z_{i+1}} K_E\left(z - z'\right) \partial_{z'} \psi_i\left(z'\right) dz' \right] \psi_j\left(z\right) dz, \tag{3.17}$$

$$Z_{ij}^r = k_0^2 \int_{z_{j-1}}^{z_{j+1}} \left[\int_{z_{i-1}}^{z_{i+1}} K_E\left(z - z'\right) \psi_i\left(z'\right) dz' \right] \psi_j\left(z\right) dz. \tag{3.18}$$

The part with the derivatives is rewritten as,

$$\begin{aligned} Z_{ij}^d &= \int_{z_{j-1}}^{z_{j+1}} \left[\partial_z \int_{z_{i-1}}^{z_{i+1}} K_E\left(z - z'\right) \partial_{z'} \psi_i\left(z'\right) dz' \right] \psi_j\left(z\right) dz \\ &= \underbrace{\left[\int_{z_{i-1}}^{z_{i+1}} K_E\left(z - z'\right) \partial_{z'} \psi_i\left(z'\right) dz' \right] \psi_j\left(z\right) \Big|_{z_{j-1}}^{z_{j+1}}}_{=0} \\ &\quad - \int_{z_{j-1}}^{z_{j+1}} \left[\int_{z_{i-1}}^{z_{i+1}} K_E\left(z - z'\right) \partial_{z'} \psi_i\left(z'\right) dz' \right] \partial_z \psi_j\left(z\right) dz, \end{aligned} \tag{3.19}$$

where it is assumed that $\psi_j(z)$ vanishes at the integral boundaries.

By performing the transformation of Appendix A, Equation (3.18) and (3.19) can be written in the following form,

$$\Delta z^2 \int_0^2 \left\{ K_E\left(\Delta z[m + s]\right) + K_E\left(\Delta z[m - s]\right) \right\} \gamma\left(s\right) ds, \tag{3.20}$$

with

$$\gamma\left(s\right) = \frac{1}{2} \int_{s-2}^{2-s} \psi_0\left(\frac{1}{2}(s' + s)\right) \psi_0\left(\frac{1}{2}(s' - s)\right) ds'. \tag{3.21}$$

In Equation (3.21), $\psi_0(z)$ represent also the partial derivative form of the testing function.

3.3 Basis and testing functions

In the previous section there are requirements stated, the first is that basis and testing functions should be identical (Galerkin's method), the second is that its value should be zero at the boundaries. From the literature, it is known that there are four generally expansion functions used in Galerkin's method,

1. Delta functions

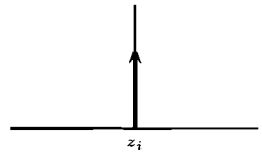

Figure 3.1: Delta function

$$\psi_i(z) = \delta(z - z_i) \quad (3.22)$$

$$\int_{-\infty}^{\infty} \delta(z - z_i) f(z) dz = f(z_i). \quad (3.23)$$

2. Pulse functions

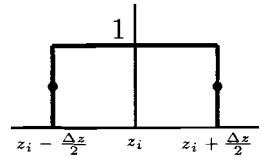

Figure 3.2: Pulse function

$$\psi_i(z) = \begin{cases} 1 & |z - z_i| < \frac{\Delta z}{2} \\ \frac{1}{2} & |z - z_i| = \frac{\Delta z}{2} \\ 0 & |z - z_i| > \frac{\Delta z}{2} \end{cases}. \quad (3.24)$$

3. Triangle functions

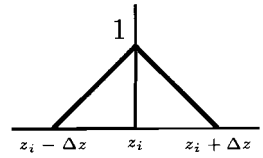

Figure 3.3: Triangle function

$$\psi_i(z) = \begin{cases} 1 - \frac{|z - z_i|}{\Delta z} & |z - z_i| \leq \Delta z \\ 0 & |z - z_i| > \Delta z \end{cases}. \quad (3.25)$$

4. Trigonometric functions

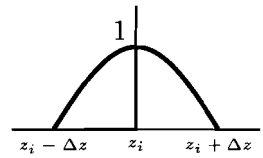

Figure 3.4: Trigonometric function

$$\psi_i(z) = \begin{cases} \cos\left(\frac{\pi(z - z_i)}{2\Delta z}\right) & |z - z_i| \leq \Delta z \\ 0 & |z - z_i| > \Delta z \end{cases}. \quad (3.26)$$

From these testing functions, only number 3 and 4 comply with the constraints discussed before.

For testing the impact of choice of basis and testing functions, we also use an extra function of the following trigonometric form

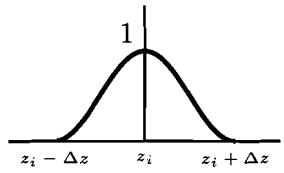

Figure 3.5: Squared cosine function

$$\psi_i(z) = \begin{cases} \cos^2\left(\frac{\pi(z-z_i)}{2\Delta z}\right) & |z - z_i| \leq \Delta z \\ 0 & |z - z_i| > \Delta z \end{cases}. \tag{3.27}$$

This squared cosine function was chosen alongside the triangle functions (3) to study differences.

3.4 Tackling the Green's function singularity

The kernel of the form $(\exp(-\imath R) - 1 + 1)/R$ can be split up into two parts. The $1/R$ part which determines the resolution or the segmentation density. With respect to the resolution of the solution, the remaining term, $(\exp(-\imath R) - 1)/R$, is less important.

The "reduced kernel" of Equation (2.28) can be calculated numerically with the Simpson rule. The $1/R$ part determines the major part of the solution. This part can be calculated analytically, but for the "reduced kernel" it is handled numerically. It is noted that this numerical approach is performed accurately enough.

The "exact kernel" of Equation (2.31) can also be split up into two parts. The denominator once again determines the resolution. Here, the denominator has an analytical solution for the ϕ-integrand, an ellipticK function. The z-integrand of the denominator is calculated numerically with the "quadpack" function "qaws", for the logarithmic singularity at the self patches. The remaining parts of the denominator are integrated with the Simpson rule. The remaining term is integrated with a 2D Simpson-quadrature rule.

From the literature, it is known that the one over the square root term is the part of the kernel which determines the resolution of the solution [25]. The maximum number of samples that produces a correct answer is called the resolution of the solution. The minimum number of samples that produces a correct answer depends on the used frequency.

3.5 Source implementation

The source is implemented with the most common form there is, the delta-gap voltage source. This source is defined as the voltage between the feed points,

see Figure 2.2. The electric field in the gap can then be defined as

$$E_z(\mathbf{r}, \omega) = -V_a \delta(z - z_g), \tag{3.28}$$

with V_a the applied voltage and z_g the location of the source. The latter equation is combined with Equation (3.12).

The impedance, Z, can be calculated as follows

$$Z = \frac{V_a}{I_g}, \tag{3.29}$$

where I_g represents the current at the feed point, located at z_g.

Chapter 4

Validation of the developed code

Before the stability analyses was started, the newly programmed code for this thesis has been validated by known working and established codes. Therefore, the code is compared with three established codes, the first is the NEC2 code [3] with the "extended kernel flag" turned off, this because this option is not well documented. The other two codes are Hallén [30] and Pocklington [29] based codes. All codes are programmed in double precision except for the NEC2 code, which is programmed in single precision. The new code is verified with three tests. In the first test, the basis functions of the code are squared cosine functions. For the second test, the basis functions are triangles. In the last test the basis functions are triangles and the wire radius is chosen much thicker. For all comparisons of the currents in this chapter, the frequency is chosen to be $f = 100$ MHz. For the impedance plots, the frequency is swept from 50 until 150 MHz in steps of 10 MHz. The wire has a length of $L = 1.5$ m and the wire radius is equal to $a = 1$ mm. This is the case for all tests, except the last one, where the wire radius is equal to $a = 5$ cm. In the results present in this chapter, EK denotes the "exact kernel" and RK is used to indicate "reduced kernel". The reference codes are denoted by NEC2, Hal and Pock for the NEC2, Hallén and Pocklington based codes, respectively. From the NEC manual [3] an engineering stability criterium is given:

$$N \leq \frac{L}{2a}, \tag{4.1}$$

that has been adopted with the analysis.

The term, resonance frequency, is the frequency corresponding with a half wave length in vacuum or free space. The antenna is in resonance for the frequency where the imaginary part of the impedance is zero. The frequency of a half-wave dipole is lower due to the influence of the finite thickness of the wire. This fact has no influence on the discussions.

4.1 Squared cosine basis and testing functions

In this section, the squared cosine basis and testing function, which can be found in Equation (3.27), have been implemented. The plots of the current are given in Figure 4.1 and Figure 4.2, for 22 and 100 samples, respectively.

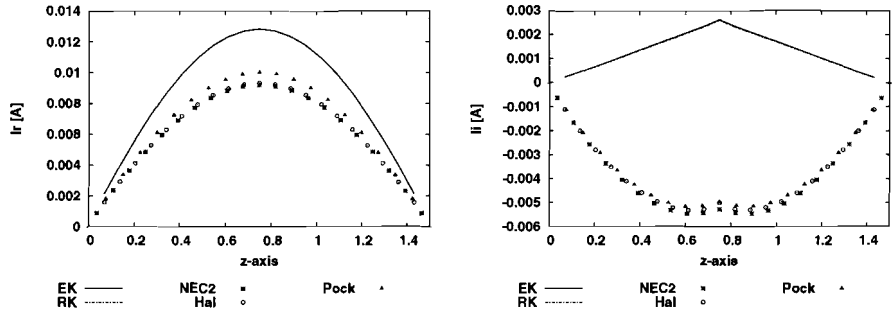

(a) The real part. (b) The imaginary part.

Figure 4.1: The current of a thin wire with $L = 1.5$ m and $a = 1$ mm. Simulated for $f = 100$ MHz and $N = 22$ squared cosine basis functions.

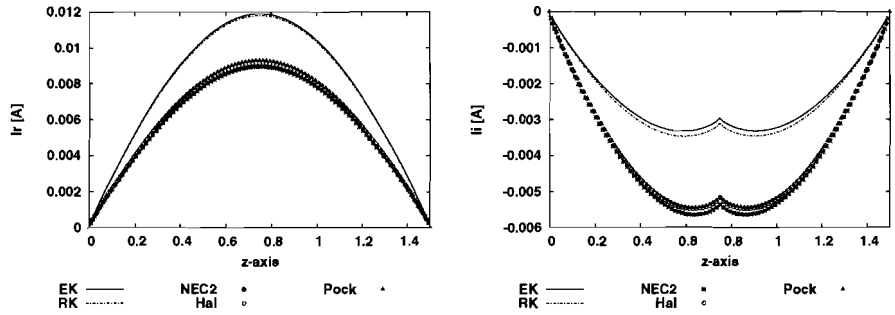

(a) The real part. (b) The imaginary part.

Figure 4.2: The current of a thin wire with $L = 1.5$ m and $a = 1$ mm. Simulated for $f = 100$ MHz and $N = 100$ squared cosine basis functions.

From the currents, it is clearly observed that the real part of RK and EK values has the right shape but the wrong value, compared with the reference codes. The imaginary part of the RK and EK code has the wrong value and shape with 22 samples. With 100 samples the shape tends to follow the results of the reference cards. The next discussion is about the impedance plots, which are depicted for 22 and 100 samples in Figure 4.3 and Figure 4.4, respectively.

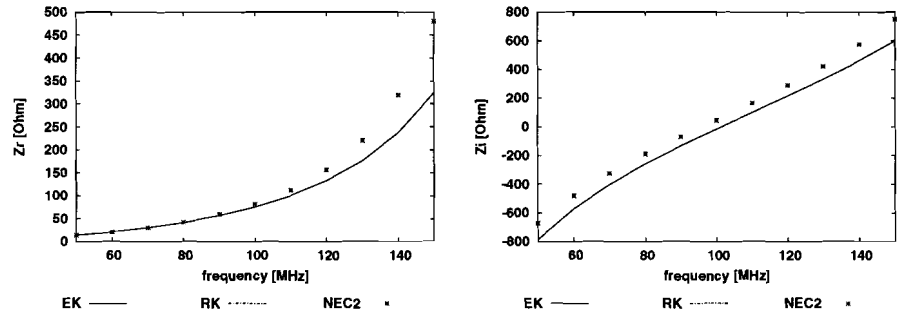

(a) The real part. (b) The imaginary part.

Figure 4.3: The impedance of a thin wire with $L = 1.5$ m and $a = 1$ mm. Simulated with $N = 22$ squared cosine basis functions.

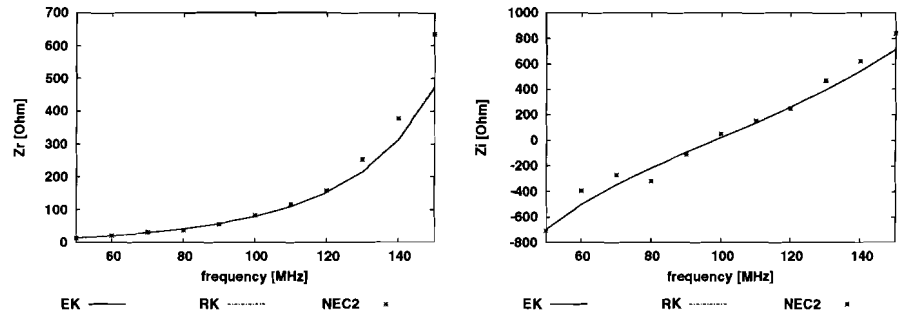

(a) The real part. (b) The imaginary part.

Figure 4.4: The impedance of a thin wire with $L = 1.5$ m and $a = 1$ mm. Simulated with $N = 100$ squared cosine basis functions.

The impedance values of the RK and EK code are correct for the frequencies below resonance, $f = 100$ MHz. Above resonance the deviation is the largest for $N = 22$. The imaginary part shows too a low value for 22 samples. For $N = 100$, the impedance is correct for the frequencies below resonance. This with an extra note, that the observations made are within the details of the impedance plots. The details perceived from these plots are less then the ones perceived in the graphs of the currents.

4.2 Triangle basis and testing functions

The implementation discussed in this section uses the triangle function from Equation (3.25) as basis and testing functions. The different solutions of the currents are compared in Figure 4.5 and Figure 4.6, respectively, and will be discussed below.

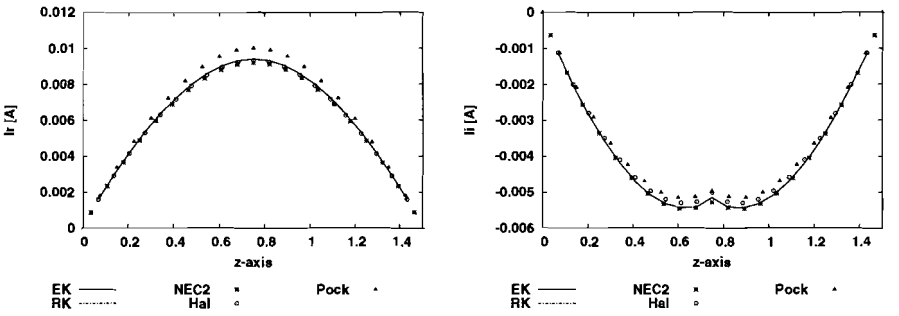

(a) The real part. (b) The imaginary part.

Figure 4.5: The current of a thin wire with $L = 1.5$ m and $a = 1$ mm. Simulated for $f = 100$ MHz and $N = 22$ triangle basis functions.

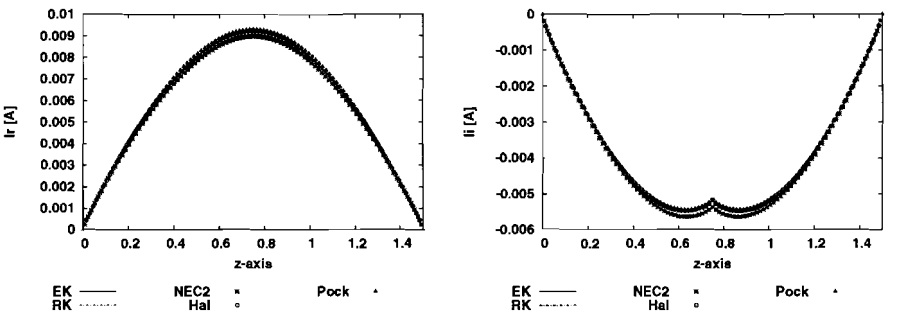

(a) The real part. (b) The imaginary part.

Figure 4.6: The current of a thin wire with $L = 1.5$ m and $a = 1$ mm. Simulated for $f = 100$ MHz and $N = 100$ triangle basis functions.

Comparing the shape and magnitudes of the results of the developed code with the ones of NEC2 and the other codes, shows us that the shape and values are in good agreement for both sample values. Next the impedances plotted in Figure 4.7 and Figure 4.8 are compared with each other.

The impedance values calculated by the code are the same for 22 samples. The impedance values in the plots made with 100 samples are more or less the same as the ones obtained from the reference code, NEC2. We clearly observe that the NEC2 code gives inaccurate results for the imaginary part of the impedance for 100 samples, when compared to the plots created with 22 samples. The deviation

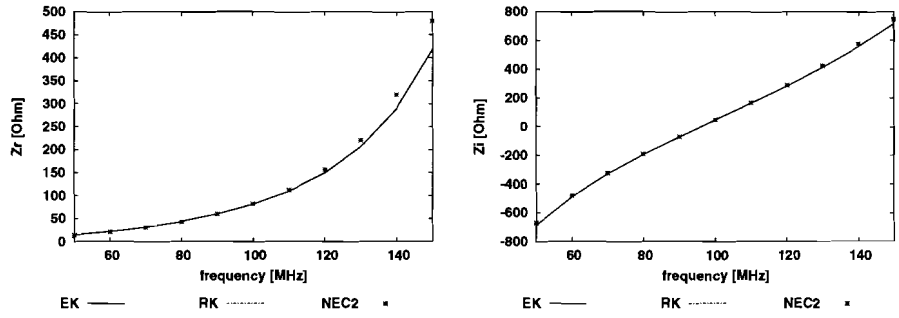

(a) The real part. (b) The imaginary part.

Figure 4.7: The impedance of a thin wire with $L = 1.5$ m and $a = 1$ mm. Simulated with $N = 22$ triangle basis functions.

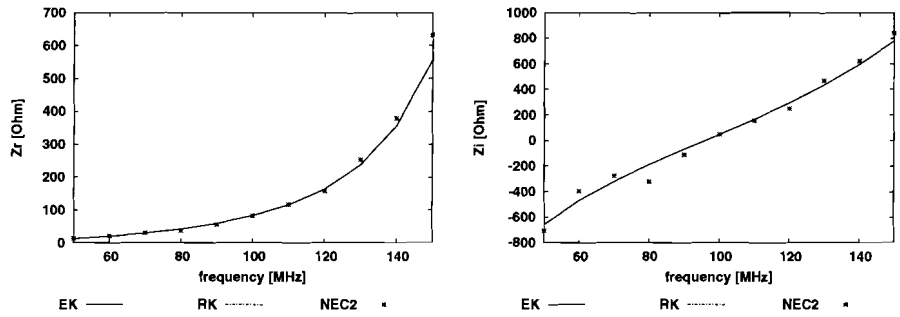

(a) The real part. (b) The imaginary part.

Figure 4.8: The impedance of a thin wire with $L = 1.5$ m and $a = 1$ mm. Simulated with $N = 100$ triangle basis functions.

between the values of some frequencies is more than 100 %.

4.3 Thick wire, $L = 1.5$ m and $a = 5$ cm

In this section, the results of the "reduced kernel" for a badly configured wire will be shown. For this example is chosen, a wire with a length of 1.5 m, a radius of 5 cm which and divided into 100 segments. This is in agreement with Equation (4.1). For such a wire, it is observed that numerical errors are introduced to the solution. The simulation is carried out for $f = 100$ MHz, and the calculated current is shown in Figure 4.9. The basis functions used here are triangles.

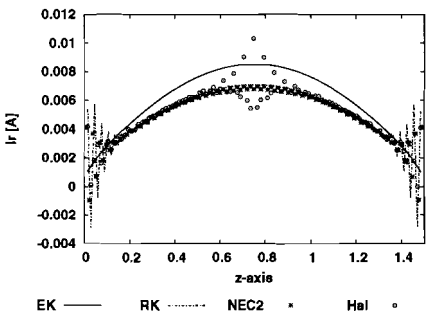

(a) The real part.

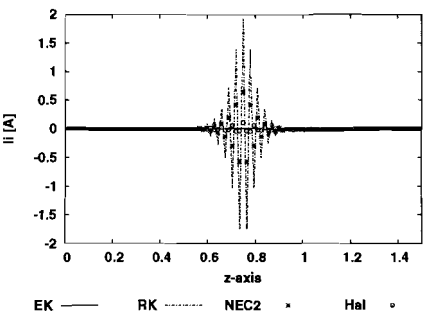

(b) The imaginary part.

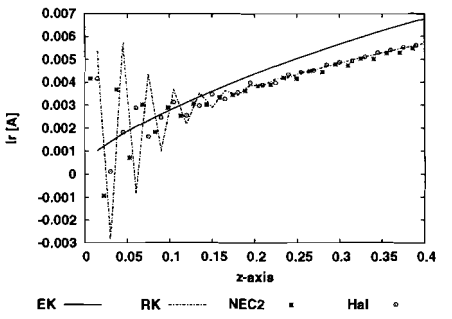

(c) The real part (zoomed).

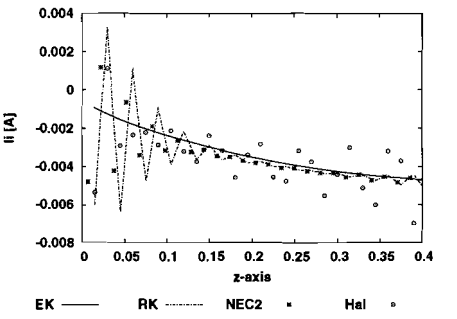

(d) The imaginary part (zoomed).

Figure 4.9: The current of a thick wire with $L = 1.5$ m and $a = 5$ cm. Simulated for $f = 100$ MHz and $N = 100$ triangle basis functions.

The results in Figure 4.9 show us that the Hallén code, NEC2 and RK code give rise to "oscillating" effects in the current near the end-faces of the wire and the feeding point. This is off course an unwanted effect.

4.4 Conclusions

From the basis and testing functions considered in this study the triangle basis and testing function produces the most accurate results for the currents and the impedances. The squared cosine functions fail to follow the shape of the current accurately enough. Especially at the end faces of the wire where the current has a square root behaviour [8] and [21, Theorem 3.2]. Hence, the calculated currents by using squared cosine functions are incorrect. The results of Section 4.3 acknowledge that reference codes that were used are based on the "reduced kernel".

Chapter 5

Stability research

The comment about the resonance frequency, f_r, of the previous chapter is still valid.

In this chapter the triangle function is used for the basis and testing function to obtain the current in all configurations studied. The stability research started for a wire with a length $L = 0.5$ m and a radius of $a = 5$ mm. The current is depicted in Figure 5.1 for $f = 300$ MHz and $N = 128$ segments. 128 Segments result in an unstable solution, according to Equation (4.1).

The demands of a stable computational model are that the current does not give rise to oscillating effects at the source or end faces of the wire, furthermore the impedance should be a good estimate of the physical one. The stability of the computational model lies within the system matrix, Z. This is due to one reason; the current is the unknown and the source matrix is known, the source matrix is, for practical purposes stable enough. Therefore, to obtain the stability of the model, we have the choice from a limited set of matrix operations: the determinant, condition number and the singular values. These operations are all related quantities.

In some figures, the horizontal axes has the following title, N[#], this represent the array index of the value of the vertical axes.

In the imaginary part of the current, the values around the source parts oscillate in the "reduced kernel" (RK) case. This is not due to a bad condition number, which is approximately 800 for the EK and 400 for the RK. A condition number lower than the inverse of the machine precision is an indication that the matrix can be inverted easily. A downside of the condition number is that it changes when the length, radius and number of segments changes, and indicates only whether the matrix becomes singular or not.

Another matrix parameter to investigate is the sorted singular values, from largest to lowest value, depicted in Figure 5.2.

The shapes and magnitudes of the singular values are different for the EK in comparison to the RK. Therefore, conclusions attributed to the sorted singular values from only one kernel cannot be easily drawn without comparing them to the ones of the other kernel. This also complies with the plots of Figure 5.3.

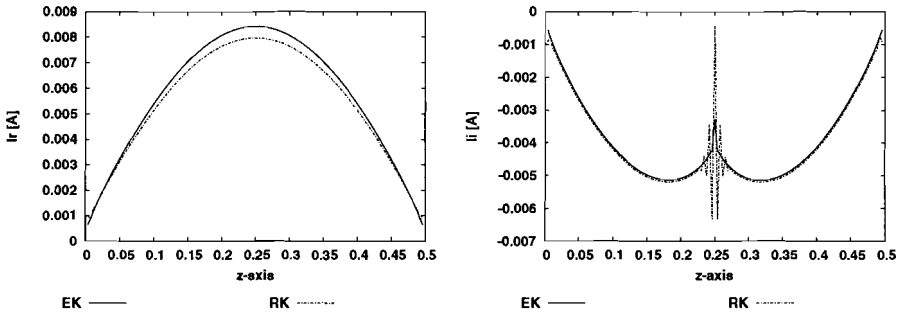

(a) The real part. (b) The imaginary part.

Figure 5.1: The current along a wire with $L = 0.5$ m and $a = 5$ mm for $f = 300$ MHz and 128 segments.

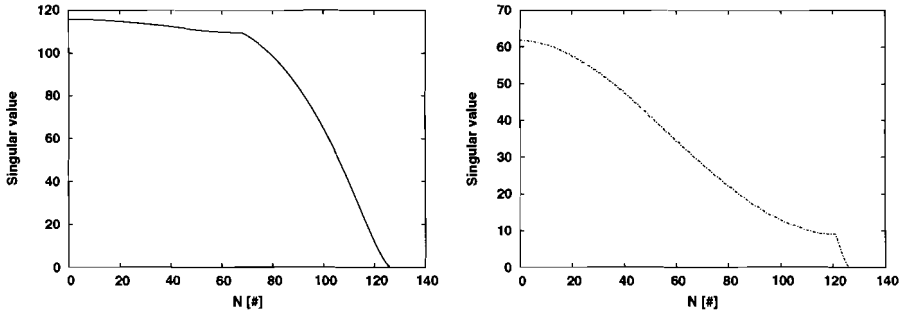

(a) The "exact kernel". (b) The "reduced kernel".

Figure 5.2: The sorted singular values of a wire with $L = 0.5$ m and $a = 5$ mm for $f = 300$ MHz and 128 segments.

The examples plotted in Figure 5.3 were ideas to obtain stability information via the matrix.

The derivative of the singular values is determined at position n, $s'[n] = s[n+1] - s[n-1]$ and a special trick for s[0] and the last value. The second order derivative is determined by $s''[n] = s[n+1] - 2s[n] + s[n-1]$. The FFT of the singular values is created by doing a FFT operation on the complete array of the singular values.

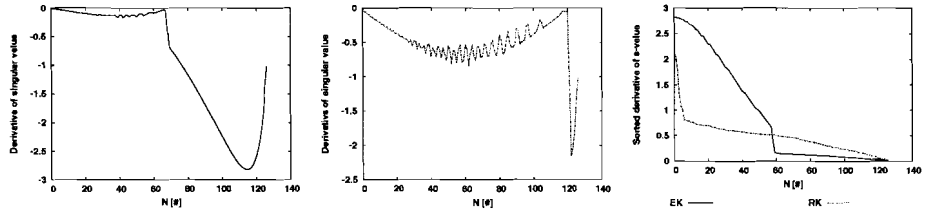

(a) The derivative of the s-values (EK).

(b) The derivative of the s-values (RK).

(c) The derivative of the s-values, sorted.

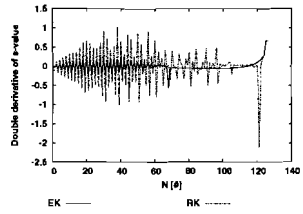

(d) The second derivative of the s-values.

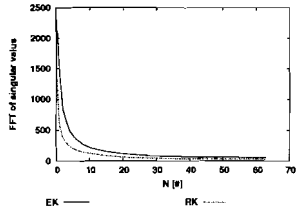

(e) The FFT of the singular values.

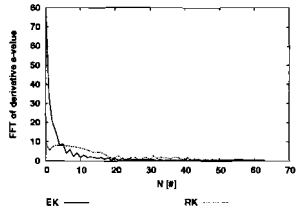

(f) The FFT of the derivative s-values.

Figure 5.3: The singular value operations on a wire with $L = 0.5$ m and $a = 5$ mm for $f = 300$ MHz and 128 segments.

One operation that gives us a good estimate whether the solution is robust or not, is the spatial Fourier transform of the current, depicted in Figure 5.4. These results do not contribute to earlier findings, because it shows that there are higher order frequencies in the current solution.

In this study indications are that the best estimate is obtained by determining the percentage of the number of singular values above a certain threshold. This threshold is chosen as the mean value of the singular values. If more than 50 % of the singular values lie above the threshold, the solution is found to be stable. An extra advantage is that this exercise has a more or less physical representation. It represents the number of participating "sources" to the solution. This assumption is tested for 3 configurations.

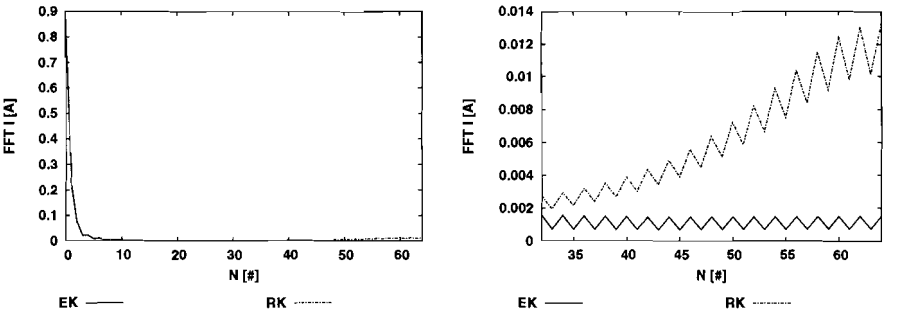

(a) The complete domain.

(b) Zoomed in at the higher frequencies of the spatial Fourier.

Figure 5.4: The spatial Fourier transform of the current for a wire with $L = 0.5$ m and $a = 5$ mm for $f = 300$ MHz and 128 segments.

5.1 Wire, $L = 0.5$ m and $a = 5$ mm

In this section, a selection of tests performed on a wire with the following dimensions $L = 0.5$ m, $a = 5$ mm and $f = 300$ MHz will be discussed. Within these tests the number of segments is increased from 8 until 1024. The results are depicted in Figure 5.5. It is observed that the impedance is wrong beyond 256 segments.

According to Figure 5.5(d), the results become unstable for 128 segments and almost unstable for 64 segments. Figure 5.6 confirms this finding.

5.2 Thin wire, $L = 50$ m and $a = 1$ mm

An interesting configuration to use as a test case is an extremely thin wire. This wire has the following dimensions, a length of 50 m, a radius of 1 mm and $f = 3$ MHz. The calculations with Equation (4.1), show that the results become unstable when the number of segments becomes larger then 25000 segments. In this configuration the segment number starts at 8 and ends with 1024, therefore the results remain stable. The results are presented in Figure 5.7.

After observing the pictures more closely, three phenomena are observed. The first observation is that the results produced by the "reduced kernel" concur with the results of the "exact kernel". The second observation is that the impedance values, plotted in Figure 5.7(a) and Figure 5.7(b) are within a 5 % error margin of each other and the results from Balanis [1, Section 7.3.2]. From the results of Figure 5.7(d) the next observation is made. Every computed segment number produces stable results. This is also found for the current which is depicted in Figure 5.8.

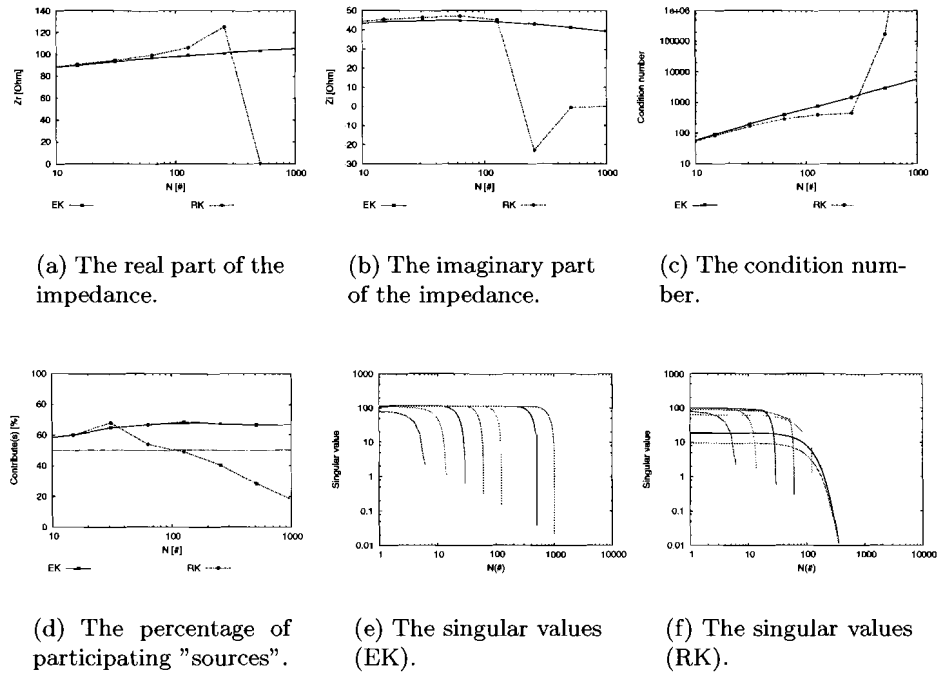

(a) The real part of the impedance.

(b) The imaginary part of the impedance.

(c) The condition number.

(d) The percentage of participating "sources".

(e) The singular values (EK).

(f) The singular values (RK).

Figure 5.5: Results of a wire with $L = 0.5$ m and $a = 5$ mm for $f = 300$ MHz.

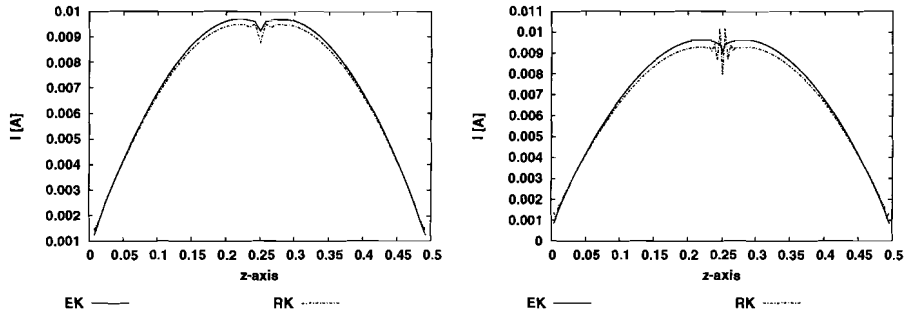

(a) 64 segments.

(b) 128 segments.

Figure 5.6: The absolute values of the current for wire of $L = 0.5$ m and $a = 5$ mm for $f = 300$ MHz.

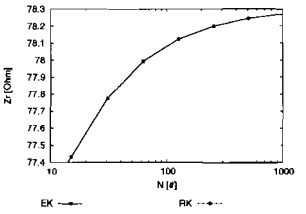

(a) The real part of the impedance.

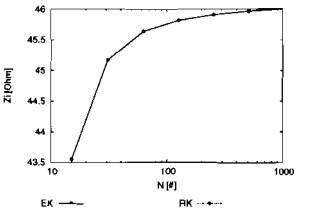

(b) The imaginary part of the impedance.

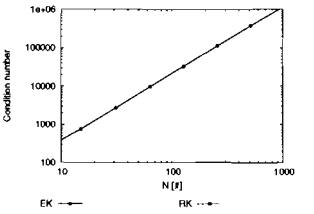

(c) The condition number.

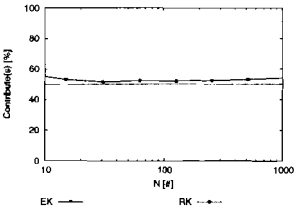

(d) The percentage of participating "sources".

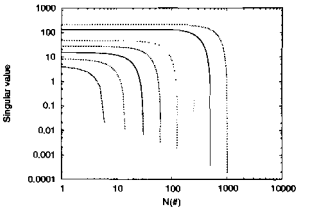

(e) The singular values (EK).

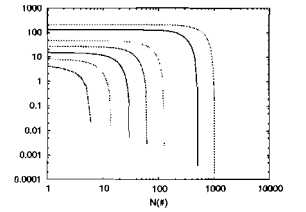

(f) The singular values (RK).

Figure 5.7: Results of a wire with $L = 50$ m and $a = 1$ mm for $f = 3$ MHz.

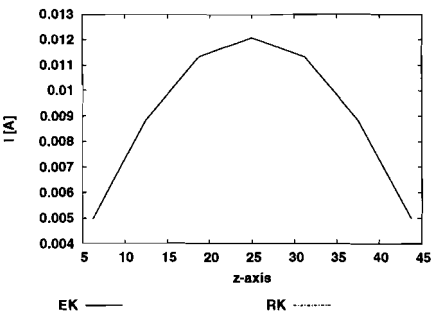

(a) 8 segments.

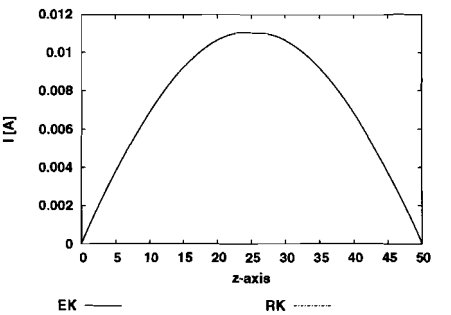

(b) 1024 segments.

Figure 5.8: The absolute values of the current for wire with $L = 50$ m and $a = 1$ mm for $f = 3$ MHz.

5.3 Thick wire, $L = 0.5$ m and $a = 1.5$ cm

The last configuration studied is a thick wire configuration, where the calculation for the "reduced kernel" should becomes unstable for N is more than 17 segments, according to Equation (4.1). The calculation for this wire is performed for 300 MHz, with $L = 0.5$ m, the wire radius $a = 1.5$ cm. The results are presented in Figure 5.9.

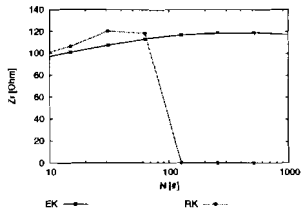

(a) The real part of the impedance.

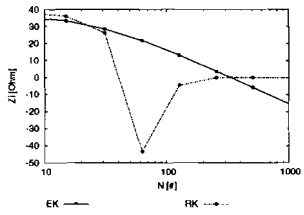

(b) The imaginary part of the impedance.

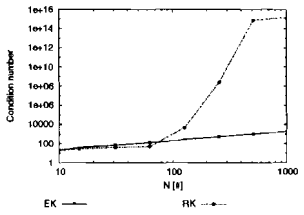

(c) The condition number.

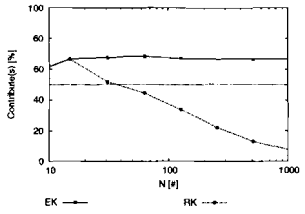

(d) The percentage of participating "sources".

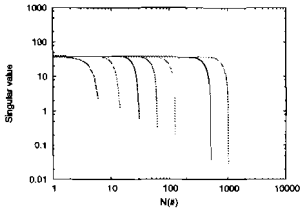

(e) The singular values (EK).

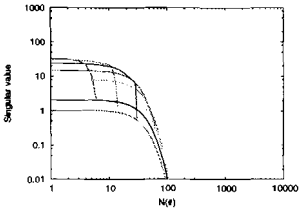

(f) The singular values (RK).

Figure 5.9: Results of a wire with $L = 0.5$ m and $a = 1.5$ cm for $f = 300$ MHz.

The real part of the impedance, Figure 5.9(a), deviates extremely for 128 segments with respect to EK. For 64 segments the imaginary part of the impedance of the RK starts to deviate from the EK, see Figure 5.9(b). The condition number does not reach the threshold value. The percentage of participating "sources" of Figure 5.9(d) indicates that 32 segments produces results that are just stable and 64 segments give unstable results. This is confirmed by the plots of the currents shown by Figure 5.10.

5.4 Conclusions

After comparing the stability plots with the calculated currents to the point where they become unstable, it may be concluded that the used stability criterium obtained of the singular values is a good estimate for that stability. Another observation is that Equation (4.1) provides a stricter stability factor, compared with the plotted values of stability criterium. Equation (4.1) is a factor 2 stricter compared to the plotted values, for example Figure 5.9(d).

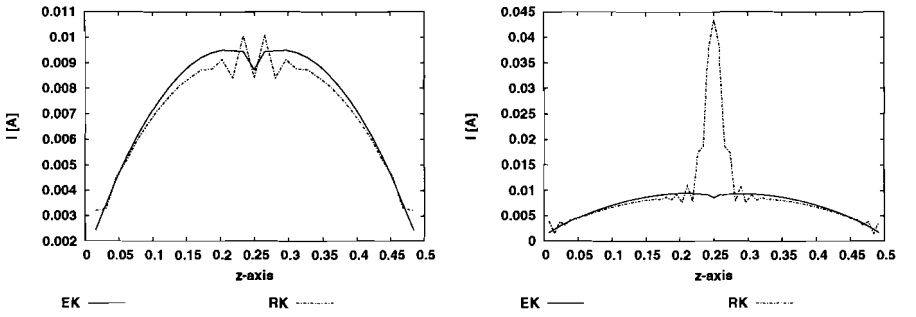

(a) 32 segments. (b) 64 segments.

Figure 5.10: The absolute values of the current for wire with $L = 0.5$ m and $a = 1.5$ cm for $f = 300$ MHz.

During this research an extra stability criterium, for which the results are not shown here, was carried out; the so-called Picard criterium. This operation shows if the obtained system matrix represents a physical existing solution. If so, the solution can be enhanced by regularisation. The Picard criterium is performed in all three cases and gave as a conclusion that all results from the RK and EK still represent a physically correct solution after regularisation.

Another test performed was the so-called Minimum Description Length (MDL), which indicates how many sources there are in a noisy environment. In our case there was no noise, so all sources participated to the solution and further implication of the MDL was cancelled.

More information of the Picard criterium and Minimum Description Length is described in Appendix B.1 and B.2, respectively.

Chapter 6

Conclusions and recommendations

6.1 Conclusions

Our goal was to investigate accuracy and reliability aspects of the numerical analysis of wire antenna structures. To achieve this, the integration of the $1/R$ term of the kernel should be calculated accurately, especially for the parts where the function has a logarithmic singularity. The integration of the $1/R$ term, in the new code, is handled with special care. The remaining term can be easily integrated numerically. Another important finding is that the basis and testing functions, which do not follow the current accurately enough in its physical behaviour, produce erroneous results as explained in Chapter 4. The basis functions for the currents at least should have a square-root like behaviour near the endpoints of the wire.

In Chapter 5, it is stated that the instabilities, "oscillation", of the "reduced kernel" are not caused by numerical inaccuracies, but by using an inferior theoretical model or incorrect discretisation of the integral equation. This result confirms suggestions made in [9, 10, 33, 31]. The condition number of the system matrix gives some sort of indication. In the case of the first oscillation effects, the condition number remained below the machine precision of the computer.

Our stability research shows that it is possible to determine a quantity that indicates the existence of a robust solution. This is possible by using the singular values of the system matrix. The following checks didn't contribute to earlier findings or weren't providing information without comparing the results of the two kernels (EK and RK):

- The sorted singular values,
- The derivative of the singular values, non-sorted and sorted,
- The second derivate of the singular values,
- The FFT of the singular values and derivative of the singular values,
- The FFT of the current,
- The so-called Picard criterium,
- The so-called Minimum Description Length.

The stability test we used determines the percentage of the number of singular values above a certain threshold. This threshold is chosen as the mean value of the singular values. If the percentage is more than 50 %, the solution is found to be stable.

Our stability test made use of singular values. From this rose the question: "What is the physical representation of the singular values?" Possible answer: "The number of participating "sources" to the solution and the interaction between each other."

6.2 Recommendations

From the previous chapters we know that the basis and testing functions should be chosen consistently with physics. In our case, triangle test and basis functions seem to be appropriate functions. However, there are more options such as parabolic and cosine. Which basis and testing function match the square-root behaviour of the current at the end faces of the wire best and makes it possible that the z-integrand of the $1/R$-term is a tabulated function, remains still a question to be answered. Probably, only the triangle and parabolic functions give a tabulated answer. A good idea is given in an article of Jones [11].

By choosing a better threshold value, the stability test can be improved. Subsequently, it should be proven that the stability test is valid for 3D-wire geometries.

From the correct answer on the question what the physical representation of the singular values is, we can provide a better threshold value. For the time being a good alternative will be the point of inflection of the sorted singular values.

To enhance the research in the stability area, there should be investigated what the best source matrix representation is. This was outside the scope and is briefly mentioned in the introduction. There it is also stated that the most promising source model is described in an article of Cui and Chew [7].

Appendix A

Variables transformation

The double integral of Equation (A.2) will be transformed into an easy integral of the basis or testing function and an integral with the kernel function [8].

$$\int_{z_{j-1}}^{z_{j+1}} \left[\int_{z_{i-1}}^{z_{i+1}} K_E\left(z - z'\right) \psi_i\left(z'\right) dz' \right] \psi_j\left(z\right) dz, \qquad \text{(A.1)}$$
$$i = 1, \ldots, N-1 \wedge j = 1, \ldots, N-1.$$

First the integration interval will be written in full, we readily obtain

$$\int_{(j-1)\Delta z}^{(j+1)\Delta z} \left[\int_{(i-1)\Delta z}^{(i+1)\Delta z} K_E\left(z - z'\right) \psi_0\left(\frac{z'}{\Delta z} - i\right) dz' \right] \psi_0\left(\frac{z}{\Delta z} - j\right) dz. \qquad \text{(A.2)}$$

Next we create three new variables $x = \frac{z}{\Delta z} - j$, $x' = \frac{z'}{\Delta z} - i$ and $m = i - j$. Then the integral can be written as

$$\Delta z^2 \int_{-1}^{1} \left[\int_{-1}^{1} K_E\left(\Delta z[x - x' - m]\right) \psi_0\left(x'\right) dx' \right] \psi_0\left(x\right) dx. \qquad \text{(A.3)}$$

The next transformation will transfer the 2D integral into a 1D integral. Therefore we introduce two new variables $s = x - x'$ and $s' = x + x'$. The integral in (A.3) becomes

$$\begin{aligned} &\frac{1}{2}\Delta z^2 \int_{0}^{2} \int_{s-2}^{2-s} K_E\left(\Delta z[s - m]\right) \psi_0\left(\frac{1}{2}(s' - s)\right) \psi_0\left(\frac{1}{2}(s' + s)\right) ds' ds \\ &+ \frac{1}{2}\Delta z^2 \int_{-2}^{0} \int_{-s-2}^{s+2} K_E\left(\Delta z[s - m]\right) \psi_0\left(\frac{1}{2}(s' - s)\right) \psi_0\left(\frac{1}{2}(s' + s)\right) ds' ds. \end{aligned} \qquad \text{(A.4)}$$

For the lower integral we change into $s = -s$ and obtain,

$$\begin{aligned}
&\frac{1}{2}\Delta z^2 \int_0^2 \int_{s-2}^{2-s} K_E\left(\Delta z[s-m]\right) \psi_0\left(\frac{1}{2}(s'-s)\right) \psi_0\left(\frac{1}{2}(s'+s)\right) ds' ds \\
&+ \frac{1}{2}\Delta z^2 \int_0^2 \int_{s-2}^{2-s} K_E\left(\Delta z[-s-m]\right) \psi_0\left(\frac{1}{2}(s'+s)\right) \psi_0\left(\frac{1}{2}(s'-s)\right) ds' ds \qquad \text{(A.5)} \\
&= \Delta z^2 \int_0^2 \left\{K_E\left(\Delta z[m+s]\right) + K_E\left(\Delta z[m-s]\right)\right\} \gamma(s)\, ds,
\end{aligned}$$

with

$$\gamma(s) = \frac{1}{2} \int_{s-2}^{2-s} \psi_0\left(\frac{1}{2}(s'+s)\right) \psi_0\left(\frac{1}{2}(s'-s)\right) ds'. \qquad \text{(A.6)}$$

Appendix B

Matrix operations

B.1 Picard criterion

Consider the following system of equations that must be solved:

$$Ax = b. \tag{B.1}$$

Where A is matrix and x and b are vectors. The quantities A and b are known, then the solution can be determined by taking the inverse of the matrix A. One way to obtain this inverse is to use Singular Value Decomposition tool (SVD).

The SVD routine provides three quantities namely, a matrix U and V^H and diagonal matrix Σ. The matrix A is decomposed as follows:

$$A = U\Sigma V^H. \tag{B.2}$$

The matrices U and V^H are composed of the normalised eigenvectors of the matrix A. The matrix Σ contains the eigenvalues of the matrix A.

In case the discrete Picard criterion ensures us if there exist a physical meaningfull solution.

Picard criterion The exact singular value decomposition coefficients $\left|u_i^H b\right|$ on the average decay to zero faster then the singular values σ_i.

Where u_i is the i-th row of matrix U. This is also described in [28, Section 4.3.1].

B.2 Minimum Description Length (MDL)

The MDL is performed on the singular values s_i of the matrix A. Where A is an $n \times n$ matrix. The MDL equation is defined as:

$$MDL(p) = (n-p)N \log \left(\frac{\frac{1}{n-p} \sum_{i=p+1}^{n} s_i^2}{\prod_{i=p+1}^{n} s_i^{2/(n-p)}} \right) + \frac{1}{2} p(2n-p) \log(N) + 2 \log(N) \tag{B.3}$$

The rank r is determined as the value of $p \in 0, 1, \cdots, n-1$ for which the MDL is minimised. An extensive explanation is given in [27, Section 4.10.2.3].

Bibliography

[1] C.A. Balanis. *Antenna Theory: analysis and design.* New York: John Wiley & Sons, Inc, 2nd edition, 1997.

[2] C.J. Bouwkamp. Hallén's theory for a straight perfectly conducting wire, used as a transmitting or receiving aerial. *Physica*, 9(7):609–631, July 1942.

[3] G.J. Burke and A.J. Poggio. *Part I: Program description, theory. Numerical Electromangnetics Code (NEC-2), Method of Moments.* Lawrence Livermore Laboratory, 1981.

[4] C.M. Buttler and D.R. Wilton. Analysis of various numerical techniques applied to thin-wire scatterers. *IEEE Transactions on antennas and propagation*, AP-23(4):534–540, July 1975.

[5] G.K. Cambrell and C.T. Carson. On Mei's integral equation of thin wire antennas. *IEEE Transactions on antennas and propagation*, AP-19(6):781–782, Nov 1971.

[6] M.F. Cátedra, R. P. Torres, J. Basterrechea, and E. Gago. *The CG-FFT method.* Boston, London: Artech House, 1995.

[7] T.J. Cui and W.C. Chew. Accurate model of arbitrary wire antennas in free space, above or inside ground. *IEEE Transactions on antennas and propagation*, 48(4):482–493, April 2000.

[8] P.J. Davies, D.B. Duncan, and S.A. Funken. Accurate and efficient algorithms for frequency domain scattering from a thin wire. *Journal of Computational Physics*, 168(1):155–183, 2001.

[9] G. Fikioris, J. Lionas, and C.G. Lioutas. The use of the frill generator in thin-wire integral equations. *IEEE Transactions on antennas and propagation*, 51(8):1847–1854, Aug 2003.

[10] G. Fikioris and T.T. Wu. On the application of numerical methods to Hallén's equation. *IEEE Transactions on antennas and propagation*, 49(3):383–391, March 2001.

[11] D.S. Jones. Note on the integral equation for a straight wire antenna. *IEE Proceedings Part H: Microwaves, Optics and Antennas*, 128(2):114–116, April 1981.

[12] G.P. Junker, A.W. Glisson, and A.A. Kishk. Accurate impedance model for antiresonant monopoles on finite ground planes. *Electronics letters*, 32(18):1632–1633, Aug 1996.

[13] G.P. Junker, A.W. Glisson, and A.A. Kishk. On the suitability of simple voltage source models for the study of mutual coupling effects. In *12th annual review of progress in applied computational electromagnetics*, pages 842–847. Montery, CA, March 1996.

[14] G.P. Junker, A.A. Kishk, and A.W. Glisson. A novel delta gap source model for center fed cylindrical dipoles. *IEEE Transactions on antennas and propagation*, 43(5):537–540, May 1995.

[15] K.K. Mei. On the integral equations of thin wire antennas. *IEEE Transactions on antennas and propagation*, AP-13:374–378, May 1965.

[16] E.K. Miller and F.J. Deadrick. Some computational aspects of thin-wire modeling. In R. Mittra, editor, *Numerical and asymptotic techniques in electromagnetics*, pages 89–127. New York: Springer-Verlag, 1975.

[17] L.W. Pearson and C.M. Butler. Inadequacies of collocation solutions to Pocklington-type models of thin-wire structures. *IEEE Transactions on antennas and propagation*, AP-23(3):295–298, March 1975.

[18] H.C. Pocklington. Electrical oscillations in wires. *Proc. Cambr. Phil. Soc.*, pages 324–332, 1897.

[19] B.P Rynne. The well-posedness of the integral equation for thin wire antennas. *IMA Journal of applied mathematics*, 49(1):35–44, 1992.

[20] B.P. Rynne. The well-posedness of the integral equations for thin antennas with distributional incident fields. *IMA Journal of applied mathematics*, 52(4):489–497, 1999.

[21] B.P. Rynne. Convergence of Galerkin method solutions of the integral equation for thin wire antennas. *Advances in Computational Mathematics*, 12(2–3):251–259, 2000.

[22] A.G. Tijhuis. Iterative techniques for the solution of integral equations in transient electromagnetic scattering. In J.A. Kong and T.P. Sarkar, editors, *PIER 5: Application of Conjugate Gradient Method to Electromagnetics and Signal Analysis*, pages 455–538. Elsevier Science Publishing Co., 1991.

[23] A.G. Tijhuis, P. Zhongqiu, and A. Rubio Bretones. Transient excitation of a straight thin-wire segment: a new look at an old problem. *IEEE Transactions on antennas and propagation*, 40(10):1132–1146, Oct 1992.

[24] L.L. Tsai. A numerical solution for the near and far fields of an annular ring of magnetic current. *IEEE Transactions on antennas and propagation*, AP-20(5):569–576, Sep 1972.

[25] M.C. van Beurden. *Integro-differential equations for electromagnetic scattering*. PhD thesis, Eindhoven University of Technology, Sept 2003.

[26] A. van Schijndel. Evaluation of available EM-codes. Technical report, Eindhoven University of Technology, 2003.

[27] C.V. van Wijk and H.W.L. Naus. Space-time signal processing. Technical Report FEL-03-I096, TNO-FEL, Nov 2003.

[28] C.V. van Wijk and H.W.L. Naus. Identification and artificial generation of magnetic signatures of vehicles. Technical Report FEL-03-A245, TNO-FEL, Jan 2004.

[29] S.H.J.A. Vossen. Mutual coupling between a wire antenna of finite conductivity and a large object. Master's thesis, Eindhoven University of Technology, 1997.

[30] S.H.J.A. Vossen. *A two-wire antenna system for detecting objects in a homogeneous dielectric half space*. PhD thesis, Eindhoven University of Technology, Apr 2003.

[31] D.H. Werner. A method of moments approach for the efficient and accurate modeling of moderately thick cylindrical wire antennas. *IEEE Transactions on antennas and propagation*, 46(3):373–382, March 1998.

[32] D.R. Wilton and C.M. Buttler. Efficient numerical techniques for solving Pocklington's equation and their relationships to other methods. *IEEE Transactions on antennas and propagation*, AP-24(1):83–86, Jan 1976.

[33] D. Wu, N. Inagaki, and N. Kikuma. Hallén type integral equation for cylindrical antennas with finite gap excitation. *IEICE Transactions on communications*, E82-B(12):2145–2152, Dec 1999.